

Beyond the Embedding Bottleneck: Adaptive Retrieval-Augmented 3D CT Report Generation

Renjie Liang¹, Yiling Ma², Yang Xing¹, Zhengkang Fan¹, Jinqian Pan¹,
Chengkun Sun¹, Li Li³, Kuang Gong¹, and Jie Xu¹

¹ University of Florida

² Yale University

³ University of Southern California

Abstract. Automated radiology report generation from 3D CT volumes often suffers from incomplete pathology coverage. We provide empirical evidence that this limitation stems from a representational bottleneck: contrastive 3D CT embeddings encode discriminative pathology signals, yet exhibit severe dimensional concentration, with as few as 2 effective dimensions out of 512. Corroborating this, scaling the language model yields no measurable improvement, suggesting that the bottleneck lies in the visual representation rather than the generator. This bottleneck limits both generation and retrieval; naive static retrieval fails to improve clinical efficacy and can even degrade performance. We propose **AdaRAG-CT**, an adaptive augmentation framework that compensates for this visual bottleneck by introducing supplementary textual information through controlled retrieval and selectively integrating it during generation. On the CT-RATE benchmark, AdaRAG-CT achieves state-of-the-art clinical efficacy, improving Clinical F1 from 0.420 (CT-Agent) to 0.480 (+6 points); ablation studies confirm that both the retrieval and generation components contribute to the improvement. Code is available at <https://github.com/renjie-liang/Adaptive-RAG-for-3DCT-Report-Generation>.

Keywords: 3D CT report generation · retrieval-augmented generation · contrastive representation analysis

1 Introduction

Three-dimensional computed tomography (CT) is central to thoracic diagnosis, yet translating volumetric findings into structured radiology reports remains labor-intensive. Recent work has explored vision-language models for this task: CT-CHAT [15] combines a contrastive 3D vision encoder with a large language model; CT-Agent [11] incorporates anatomy-aware retrieval and chain-of-thought reasoning; and BTB3D [17] replaces contrastive encoders with reconstruction-based tokenization. Despite these advances, the best reported Clinical F1 on CT-RATE remains below clinically acceptable levels, indicating that many pathological findings remain unreported.

To understand this limitation, we analyze the representation space of contrastive 3D CT embeddings. Linear probes [2] achieve AUC scores between 0.59 and 0.97 across 18 pathological findings, confirming that discriminative signals are present. However, principal component analysis shows that most variance is concentrated in only a few dimensions [1, 21], resulting in extremely low effective dimensionality; organ-level encoders exhibit similar behavior. These embeddings can therefore distinguish coarse pathological states, but they lack the capacity to represent fine-grained report semantics. Scaling the language model from 8B to 70B parameters yields no measurable improvement [17, 39], indicating that the bottleneck lies in the visual representation rather than the decoder.

When the visual channel cannot carry sufficient information, additional information must be introduced through another modality. Retrieval-augmented generation [13, 19, 23] offers a mechanism for such supplementation: retrieving reference sentences from similar cases and injecting them as context supplies the generator with details not encoded in the visual embedding. However, the reliability of this textual channel depends on the same representation that constrains generation. If the embedding lacks capacity to separate fine-grained pathological findings, image-based retrieval cannot reliably isolate relevant cases. In practice, naive static retrieval does not improve clinical efficacy and can even degrade performance.

An empirical analysis across four 3D contrastive encoders confirms this link: pathology-level retrieval precision remains low, particularly for organs with diverse findings. As a result, image-based retrieval struggles to isolate relevant findings when multiple pathologies co-occur within the same organ. Rather than replacing the encoder, as in concurrent reconstruction-based approaches [17], we retain existing contrastive models and design a controlled augmentation strategy that maximizes the utility of the textual channel while mitigating the misalignment inherited from the visual representation.

Our framework, AdaRAG-CT, introduces supplementary textual context through controlled retrieval and integrates it selectively during report generation. At the retrieval stage, we explore strategies that improve finding-level relevance beyond naive image-based retrieval. At the decoding stage, inspired by Self-RAG [3], a learned [RAG] token allows the model to trigger retrieval and condition on the returned context only when it is beneficial, trained via an oracle-mixed regime that exposes the model to both ground-truth and imperfect retrievals.

This work makes three contributions. First, we diagnose a representational bottleneck in 3D medical contrastive embeddings: a PCA analysis across four encoders reveals effective dimensionalities of only a few dimensions, far below natural-image CLIP, providing empirical evidence that the visual channel alone cannot support comprehensive report generation. Second, we propose AdaRAG-CT, an adaptive augmentation framework that compensates for this bottleneck by introducing and controlling supplementary textual information: retrieval strategies improve finding-level relevance, while a learned adaptive mechanism enables the generator to selectively utilize retrieved context. Third, with adaptive retrieval augmentation, our model achieves state-of-the-art clinical efficacy

on CT-RATE; ablation studies confirm that both the retrieval and generation components contribute to the improvement.

2 Related Work

2.1 3D Medical Report Generation

Generating free-text reports from volumetric CT data has advanced rapidly alongside large language models. CT2Rep [16] introduced the first dedicated 3D CT report-generation framework using an autoregressive transformer with relational memory; subsequent work scaled this recipe by pairing 3D CT encoders with powerful LLMs (CT-CHAT [15], Med3DVLM [42]). CT-Agent [11] augments generation with anatomy-specific LoRA and memory-based exemplar retrieval; other work explores multi-modal fusion [22, 34] or memory-driven evidence aggregation [12, 40]. Several works directly recognise the visual representation as a bottleneck and propose alternative tokenization or aggregation schemes (BTB3D [17], SAMF [18]), or pursue broader 3D understanding via multi-task pre-training (M3D [4], RadFM [41]). Our work complements this line by providing a quantitative diagnosis of *why* existing contrastive embeddings limit retrieval quality—the effective dimensionality is too low to encode fine-grained pathology semantics—and proposing an adaptive RAG framework that compensates through a textual channel rather than modifying the encoder.

2.2 Retrieval-Augmented Generation in Medical Imaging

RAG has been widely adopted in open-domain NLP [13, 24], where dense retrieval over pre-trained embeddings provides grounding for generative models. In medical imaging, retrieval-based approaches have been explored for 2D chest X-ray report generation [8, 19], typically retrieving full reports or report sections from a database and using them as templates or auxiliary inputs. These methods generally assume that retrieval quality is sufficient and focus on how to integrate retrieved content. Our analysis reveals that this assumption breaks down for 3D CT, where contrastive embeddings exhibit a systematic variance-semantic misalignment that limits cosine retrieval precision. In the NLP literature, adaptive retrieval strategies have been explored: FLARE [20] generates a tentative continuation, detects low-confidence tokens, backtracks, and re-generates with retrieved context; Self-RAG [3] trains reflection tokens to critique and select among retrieval-augmented candidates. Our approach differs in that the model emits a dedicated [RAG] token proactively during generation, triggering retrieval without backtracking or speculative rollback. The adaptive mechanism we propose, combining two-stage re-ranking with a learned retrieval trigger, addresses a problem that, to our knowledge, has not been explicitly studied in the medical RAG literature.

2.3 Representation Quality in Contrastive Vision-Language Pre-training

Contrastive learning has become the dominant paradigm for aligning visual and textual representations [25, 26, 29, 36]. Several studies have identified patholo-

gies in contrastive representation spaces: dimensional collapse, where embeddings occupy a low-dimensional subspace [21]; modality gap, where image and text embeddings cluster separately [28,31]; and feature suppression, where task-irrelevant variance dominates learned features [27,30,37,44]. In the medical domain, CT-CLIP [15] and ViSD-Boost [9] have trained 3D CT encoders with contrastive objectives on CT-RATE, but the retrieval-level consequences of their representation geometry have received little attention. Our analysis complements these works by showing that the dominant variance directions in 3D medical contrastive embeddings fail to encode pathological semantics, a finding we term *variance-semantic misalignment*, and that this property directly undermines downstream RAG pipelines.

3 Diagnosing the Representational Bottleneck in 3D CT Embeddings

We first diagnose the representational bottleneck of 3D CT contrastive embeddings and its consequences for retrieval. All experiments use the CT-RATE dataset [15] (25,692 non-contrast chest CT studies with paired reports and 18 binary pathology labels) and three families of pre-trained 3D contrastive encoders: CT-CLIP [15] and its fine-tuned variant CT-CLIP (VocabFine), FVLM [38], and ViSD-Boost [9].

3.1 Encoded but Narrow

Following Alain and Bengio [2], we train linear probes (logistic regression) on frozen representations to test whether pathology information is linearly accessible. Across the three encoders, probe AUC ranges from 0.59 to 0.97 for average-pooled embeddings across 18 pathological findings (Tab. 2), confirming that the contrastive objective successfully encodes diagnostic signals. However, high AUC does not imply rich information content. A principal component analysis [1,21] of the embedding spaces reveals that the effective dimensionality is remarkably low (Tab. 1). CT-CLIP with average pooling concentrates 90% of its variance in only 2 principal components ($\text{dim}_{90} = 2$, $\text{PR} = 1.4$); although max pooling inflates dim_{90} to 117, the participation ratio remains only 6.7, indicating that most of this spread is long-tail noise rather than signal. Consistent with this, linear probe AUC is actually lower for max pool (category-mean AUC 0.66–0.68) than for avg pool (0.73–0.75; see Tab. 2). Organ-level embeddings from ViSD-Boost and FVLM fare similarly ($\text{dim}_{90} = 4\text{--}9$ out of 256). An embedding can achieve high binary AUC (e.g., “pleural effusion present vs. absent”) using just one or two directions, yet the fine-grained semantic detail required for report generation (laterality, severity, co-occurring findings) simply cannot be encoded in so few effective dimensions. This distinction between discriminability (high AUC) and information richness (low effective dimensionality) is central to our argument: the bottleneck is not that the LLM fails to extract available information, but that *the visual channel carries too little information* to begin with. A natural-image baseline confirms the severity of this concentration: CLIP ViT-B/32 on ImageNet

Table 1: Effective dimensionality of 3D CT contrastive embeddings. $\text{dim}_{90}/\text{dim}_{95}$: number of principal components capturing 90%/95% of variance. PR: participation ratio.

Model	Embedding	Total dim	dim_{90}	dim_{95}	PR
CLIP ViT-B/32 (ImageNet)	image emb.	512	243	322	64.4
CT-CLIP (Zero-shot)	avg pool	512	2	4	1.4
CT-CLIP (Zero-shot)	max pool	512	117	194	6.7
CT-CLIP (VocabFine)	avg pool	512	1	2	1.2
CT-CLIP (VocabFine)	max pool	512	3	43	1.3
ViSD-Boost	lung	256	9	12	6.3
ViSD-Boost	heart	256	5	6	3.6
FVLM	lung	256	6	8	4.9
FVLM	heart	256	4	6	2.6

achieves $\text{dim}_{90} = 243$ and $\text{PR} = 64.4$ on the same 512-dimensional space, nearly $50\times$ higher than CT-CLIP (Tab. 1). Two factors likely explain the gap. First, natural images span visually diverse categories, encouraging the encoder to use many dimensions; chest CT volumes are structurally homogeneous, with pathological differences confined to subtle local variations, so a contrastive objective can separate most cases with very few directions. Second, existing 3D CT encoders are trained with a global contrastive loss that pairs an entire volume with an entire report, a granularity too coarse to incentivize fine-grained, finding-level representations. A scaling experiment corroborates this diagnosis: replacing the 8B LLM with a 70B variant yields Clinical F1 of 0.405 versus 0.455, showing no improvement despite an $8.75\times$ increase in generator capacity. If the bottleneck were in the decoder, a larger model should improve performance; the absence of any gain confirms that the visual channel is the limiting factor. This observation is consistent with prior findings: CT-CHAT reports near-identical metrics at 8B and 70B scales [15], and BTB3D similarly concludes that improved visual tokenization, rather than larger language backbones, is essential for 3D medical VLMs [17].

3.2 Retrieval Under the Bottleneck

The dimensional concentration identified above has direct consequences for retrieval. When most variance concentrates in a few dimensions, cosine similarity is dominated by these directions, collapsing fine-grained pathological distinctions. We measure organ-level Jaccard@10, the intersection over union of pathology label sets between the query and each of the top-10 cosine-nearest neighbours averaged over queries, and compare image-to-image, image-to-text (cross-modal), and text-to-text retrieval against an upper bound constructed from ground-truth pathology label overlap (Tab. 3). Lung retrieval is weakest ($\text{Jaccard}@10 = 0.351$): with 11 distinct findings, the Jaccard denominator grows quickly, requiring precise alignment across a combinatorially large label space. The upper bound of 0.992 for lung confirms that the database contains relevant matches—the bottle-

Table 2: Linear probe AUC on frozen contrastive embeddings.*

Finding	CT-CLIP (Zero-shot)		CT-CLIP (VocabFine)		FVLM	ViSD-Boost
	avg	max	avg	max		
<i>Lung findings (11)</i>						
Lung nodule	0.619	0.582	0.588	0.516	0.664	0.713
Mosaic attenuation	0.794	0.710	0.711	0.578	0.887	0.892
Peribronchial thick.	0.717	0.631	0.730	0.645	0.777	0.814
Consolidation	0.732	0.659	0.630	0.543	0.859	0.920
Bronchiectasis	0.679	0.605	0.624	0.564	0.752	0.790
Interlob. septal thick.	0.762	0.700	0.725	0.583	0.863	0.874
Emphysema	0.712	0.629	0.695	0.641	0.792	0.799
Atelectasis	0.680	0.627	0.667	0.561	0.738	0.797
Lung opacity	0.653	0.610	0.634	0.551	0.805	0.871
Pulm. fibrotic seq.	0.621	0.582	0.614	0.542	0.688	0.744
Pleural effusion	0.911	0.849	0.850	0.718	0.956	0.966
<i>Heart findings (2)</i>						
Cardiomegaly	0.891	0.794	0.836	0.666	0.943	0.952
Pericardial effusion	0.797	0.687	0.764	0.685	0.851	0.910
<i>Aorta findings (2)</i>						
Arterial wall calc.	0.818	0.734	0.808	0.676	0.898	0.913
Coronary artery calc.	0.812	0.737	0.797	0.664	0.879	0.903
<i>Esophagus findings (1)</i>						
Hiatal hernia	0.701	0.650	0.665	0.573	0.758	0.821
<i>Other findings (2)</i>						
Lymphadenopathy	0.688	0.621	0.648	0.586	—	—
Medical material	0.726	0.642	0.688	0.590	—	—
Macro avg	0.739	0.669	0.704	0.604	0.823	0.853

* “—”: finding outside the organ encoder’s scope.

neck lies in the representation, not the coverage. By contrast, heart (2 findings) and esophagus (1 finding) achieve much higher overlap simply because fewer labels need to agree. The aorta is an exception (Img2Img 0.741 > Txt2Txt 0.666): its pathological vocabulary (arterial and coronary calcification) overlaps substantially with the heart section, reducing text-to-text discriminability, whereas the organ-specific image embeddings remain well-separated by construction.

A clear asymmetry emerges across modalities. Text-to-text cosine similarity outperforms image-to-image retrieval for lung (0.563 vs. 0.351), heart (0.925 vs. 0.825), and esophagus (0.935 vs. 0.796), indicating that the text encoder preserves pathological semantics more effectively than the image encoder. Cross-modal retrieval (Img2Txt) is worse than image-to-image for all organs, indicating that direct cross-modal matching is unreliable in this setting. The gap between Txt2Txt and Img2Img suggests that the bottleneck originates in the image representation, not in cosine similarity per se. Conventional medical RAG systems

Table 3: Retrieval precision (Jaccard@10) by modality. Img2Img: image embedding cosine similarity. Img2Txt: image query against text database (cross-modal). Txt2Txt: text embedding cosine similarity. Upper Bound: ranking by ground-truth pathology overlap.

Organ	Img2Img	Img2Txt	Txt2Txt	Upper Bound
Lung	0.351	0.313	0.563	0.992
Heart	0.825	0.638	0.925	1.000
Esophagus	0.796	0.617	0.935	1.000
Aorta	0.741	0.617	0.666	1.000

query a text database with the image embedding (Img2Txt), which is directly constrained by this bottleneck. Text-to-text retrieval offers a way to reduce this dependence, suggesting that retrieval strategies leveraging partial text may be more robust than purely image-based approaches. These observations motivate the adaptive framework introduced in Sec. 4.

4 Method: AdaRAG-CT

AdaRAG-CT operates on top of a base vision-language model and augments it with adaptive retrieval-augmented generation. We describe each component below and connect design choices to the diagnostic findings of Sec. 3.

4.1 Base Model

We adopt a LLaVA-style architecture [33] where a pre-trained LLM (Llama-3.1-8B-Instruct and Llama-3.3-70B-Instruct [14]) receives visual input through learned projectors. Each 3D CT volume is represented by $K = 5$ embeddings: a global max-pooled embedding $\mathbf{v}_{\text{global}} \in \mathbb{R}^{512}$ from CT-CLIP and four organ-specific embeddings $\mathbf{v}_o \in \mathbb{R}^{256}$ ($o \in \{\text{lung, heart, esophagus, aorta}\}$) from ViSD-Boost. Each embedding is projected independently as

$$\mathbf{h}_o = \text{MLP}_o(\mathbf{v}_o), \quad \mathbf{h}_o \in \mathbb{R}^{d_{\text{LLM}}}, \quad (1)$$

where MLP_o is a 2-layer projector specific to organ o . The resulting visual tokens $\{\mathbf{h}_o\}_{o=1}^K$ are incorporated into the input token sequence as visual context for the LLM. This base model, without any retrieval augmentation, serves as our primary baseline.

4.2 Organ-Indexed Sentence Database

We construct an organ-indexed sentence database from all training reports. Each report is first split into individual sentences using NLTK sentence tokenisation. Every sentence is then annotated with its corresponding organ label (lung, heart, esophagus, aorta) and associated pathology findings, yielding approximately 572K sentences in total across both Findings and Impression sections.

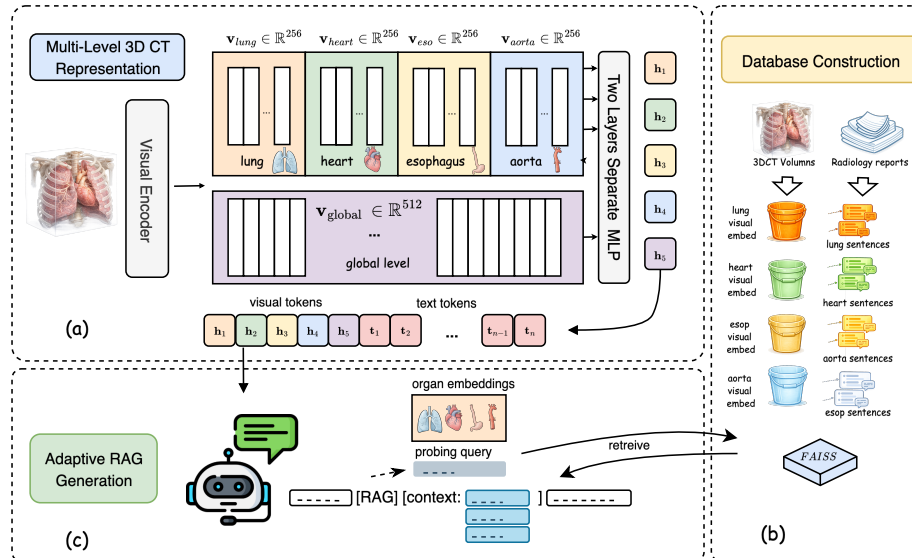


Fig. 1: Overview of AdaRAG-CT. (a) A 3D CT volume is encoded into a global embedding (CT-CLIP) and four organ-specific embeddings (ViSD-Boost), which are projected into the LLM input space as visual tokens. (b) An organ-indexed sentence database is built from training-set reports and indexed with FAISS for efficient retrieval. (c) During report generation, the LLM autonomously emits a [RAG] token when it needs external evidence; retrieved sentences are then injected into the context before the model continues generating.

To represent each sentence, we employ a text encoder based on BiomedVLP-CXR-BERT [7], followed by a learned 256-dimensional projection layer. The text encoder and projection layer are fine-tuned using a contrastive image-text objective, with frozen organ-level image embeddings serving as anchors. All sentence embeddings are stored in per-organ FAISS indices to enable efficient nearest-neighbour retrieval. Organ-level image embeddings from the training set are similarly indexed for coarse candidate retrieval.

4.3 Adaptive Retrieval Training

Following Self-RAG [3], we introduce a special [RAG] token into the vocabulary. Rather than injecting context at predetermined positions, the model learns to generate [RAG] autonomously when it determines that external context would be beneficial. To identify where [RAG] should appear during training, we run the base model on ground-truth reports and compute per-sentence perplexity; sentences exceeding a fixed percentile threshold are marked as retrieval targets. For each target, context sentences are precomputed offline via image-based coarse filtering followed by text-to-text re-ranking. Final candidates are selected using Maximal Marginal Relevance (MMR) [10]:

$$\text{MMR}(d_i) = \lambda \cdot \text{sim}(d_i) - (1 - \lambda) \cdot \max_{d_j \in \mathcal{S}} \text{BLEU-2}(d_i, d_j), \quad (2)$$

where $\text{sim}(d_i)$ is the cosine similarity score and \mathcal{S} is the set of already-selected sentences. Each retrieval target then receives either ground-truth reference sentences (oracle context) with probability p_{oracle} , or real retrieval results (noisy context) otherwise. This oracle-mixed regime exposes the model to high-quality signals while building robustness to imperfect retrieval. Oracle context is used only during training; injected context tokens are masked from the generation loss.

4.4 Adaptive Retrieval Inference

During autoregressive generation, whenever the model emits [RAG], it continues to generate the next sentence, which is then used as the retrieval query. The retrieved sentences are formatted and injected into the context, the initial generation is rolled back, and the model regenerates the sentence with the retrieved context. We explore two retrieval strategies for supplying candidate sentences. As shown in Fig. 2, both yield comparable generation quality, reinforcing that the adaptive [RAG] mechanism is the primary driver of improvement. Both strategies use MMR (Eq. (2)) for final candidate selection with $K_{\text{fine}} = 3$.

Two-Stage retrieval. Given the organ currently being described, we first retrieve the $K_{\text{coarse}} = 20$ most similar training samples using image embedding cosine similarity, collecting all their sentences for the same organ as a candidate pool. This vision-guided stage narrows the search from the full database to patient-relevant candidates. Candidates are then re-ranked and selected via MMR (Eq. (2)) against the current query sentence.

Text2Text retrieval. We retrieve directly from the full per-organ sentence database using text-to-text cosine similarity, with the model’s partial generation as query. Candidates are selected via MMR (Eq. (2)).

Together, these components compensate for the limited visual channel through controlled textual augmentation.

5 Experiments

5.1 Setup

Dataset. All experiments use CT-RATE [15], comprising 25,692 non-contrast chest CT studies from 21,304 patients, each paired with a free-text radiology report containing both Findings and Impression sections. We use the concatenation of both sections as the generation target, and follow the official train/validation/test split provided by CT-RATE.

Table 4: Report generation performance on the CT-RATE validation set. Baseline numbers are from original publications.

Method	Params	Clinical Efficacy			NLP				LLaMA Score
		F1	P	R	B-1	B-4	R-L	MET	
CT2Rep [16]	—	0.160	0.435	0.128	0.372	0.213	—	0.197	—
Merlin [6]	7B	0.160	0.295	0.112	0.231	0.099	—	0.148	—
CT-CHAT [15]	8B	—	—	—	0.494	—	0.584	0.311	7.440
CT-CHAT [15]	70B	0.184	0.450	0.158	0.498	—	0.581	0.311	7.429
BTB3D [17]	8B	0.258	0.260	0.260	0.439	0.213	—	0.223	—
SAMF [18]	3.8B	—	—	—	0.440	0.261	0.417	0.417	7.165
CT-Agent [11]	—	0.420	0.423	0.477	0.502	0.231	0.490	0.425	—
Ours (base)	8B	0.455	0.474	0.469	0.463	0.205	0.315	0.206	7.30
AdaRAG-CT	8B	0.480	0.502	0.520	0.496	0.242	0.354	0.246	7.75
Ours (base)	70B	0.405	0.468	0.373	0.449	0.213	0.334	0.208	7.10
AdaRAG-CT	70B	0.426	0.483	0.413	0.497	0.250	0.361	0.232	7.53

Note: We also reproduce several baselines under our unified evaluation protocol in Tab. 10.

Metrics. Following the CT-RATE evaluation protocol [15], we adopt Clinical Efficacy as the primary metric. A RadBERT-based classifier [43] extracts 18 binary pathological finding labels (e.g., lung nodule, pleural effusion, cardiomegaly) from each generated report. These predictions are compared against the dataset-provided ground-truth annotations to compute per-finding Precision, Recall, and F1. We report the support-weighted macro average as Clinical Precision (Clin-P), Clinical Recall (Clin-R), and Clinical F1 (Clin-F1). We also report BLEU [35], ROUGE-L [32], and METEOR [5] for textual overlap.

Baselines. We compare against prior methods on CT-RATE report generation: CT2Rep [16], an encoder-decoder with relational memory; Merlin [6], a 7B VLM for 3D CT understanding; CT-CHAT [15], which pairs a CT-ViT encoder with Llama-3.1 (8B/70B) via attention pooling; BTB3D [17], which uses reconstruction-based visual tokenization; SAMF [18], a 2D–3D feature fusion approach; and CT-Agent [11], an agent-based pipeline with chain-of-thought reasoning. All baseline numbers are taken from the original publications. We also report our own base model (no RAG) at 8B and 70B scales, trained in two stages: organ-specific projectors with frozen LLM weights, followed by full LoRA fine-tuning.

5.2 Main Results

Table 4 presents the main comparison. Our 8B base model obtains a Clinical F1 of 0.455 without retrieval. Scaling the LLM to 70B does not improve this figure; in fact, the 70B base model scores only 0.405, consistent with the PCA analysis showing that the visual channel carries only 2–9 effective dimensions (Sec. 3.1). Both models read the same impoverished visual representations, so the larger decoder has no additional signal to exploit—the bottleneck is representational, not generative. Retrieval augmentation benefits both scales: the 8B model improves from 0.455 to 0.480 (+0.025) and the 70B model from 0.405 to

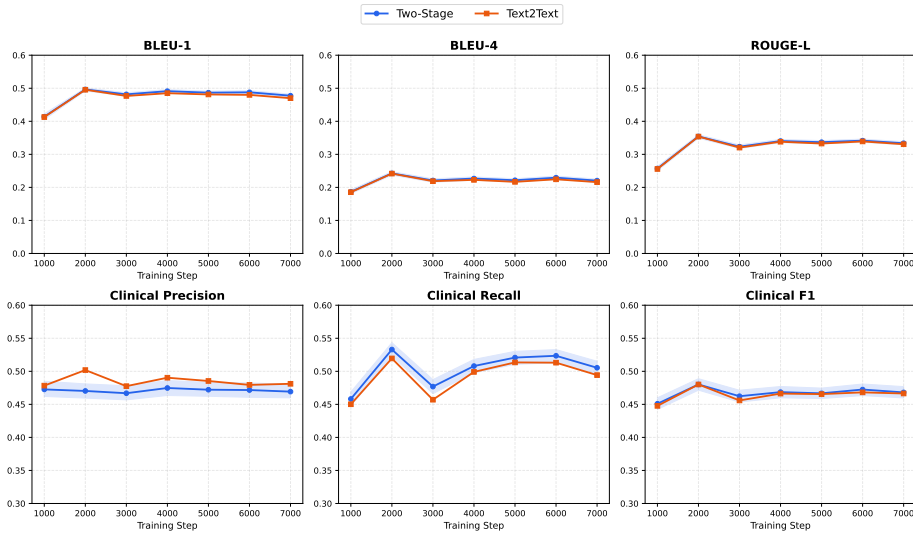


Fig. 2: Six evaluation metrics across training steps for Two-Stage and Text2Text retrieval pipelines on the 8B model, with bootstrap 95% confidence intervals.

0.426 (+0.021), confirming that the textual channel supplies information absent from the visual input. The 8B AdaRAG-CT (0.480) surpasses CT-Agent (0.420) and substantially outperforms CT-CHAT 70B (0.184) in Clinical F1, while also improving NLP metrics and LLaMA Score across the board.

5.3 Retrieval Pipeline Comparison

Figure 2 shows that both pipelines yield stable performance throughout training, with Clinical F1 virtually identical at every step and bootstrap confidence intervals consistently overlapping, confirming robustness to checkpoint selection. A closer look at the precision–recall decomposition reveals a mild trade-off: Two-Stage retrieval, which first narrows candidates via image similarity before text re-ranking, tends to surface a broader set of organ-level findings and thus favours recall; Text2Text retrieval, which matches directly against the model’s partial generation, returns more topically precise context and favours precision. These complementary biases cancel out in F1, reinforcing that the adaptive [RAG] utilization mechanism—not the retrieval pipeline—is the primary driver of improvement. This pattern is consistent with the bottleneck hypothesis: because any sufficiently relevant textual context substantially compensates for the impoverished visual signal, the marginal benefit of a more precise retrieval strategy is small.

5.4 Context Utilization Ablation

Table 5 ablates the context injection strategy while holding the retrieval pipeline fixed. The No RAG baseline (0.462) reflects the RAG-trained model’s own gener-

Table 5: Context utilization ablation (8B model). All variants share the same retrieval pipeline; Δ is relative to the No RAG baseline.

Utilization Strategy	Clin-F1	Δ	BLEU-4	ROUGE-L
No RAG	0.462	—	0.228	0.349
Fixed-interval ($N=3$)	0.453	-0.009	0.192	0.307
Fixed-interval ($N=5$)	0.494	+0.032	0.209	0.329
Fixed-interval ($N=7$)	0.482	+0.020	0.228	0.346
Adaptive RAG (ours)	0.480	+0.018	0.242	0.354
- context (OOD)	0.402	-0.060	0.122	0.228

ation capability without retrieval context at inference, which differs slightly from the base model in Tab. 4 (0.455) that was trained without the RAG objective. Fixed-interval injection is sensitive to the choice of N : injecting too frequently ($N=3$) hurts performance below baseline, while $N=5$ maximises Clinical F1 (0.494) at the expense of NLP quality, and $N=7$ strikes a middle ground. This sensitivity to N highlights a practical limitation of fixed-interval strategies—the optimal frequency is dataset-dependent and requires separate tuning. Adaptive RAG resolves this by learning to trigger retrieval selectively: it achieves competitive Clinical F1 (0.480, +0.018) without any frequency hyperparameter, and consistently outperforms all fixed-interval variants on BLEU-4 and ROUGE-L. On average, the model emits 1.5 [RAG] triggers per report, confirming that retrieval is used sparingly and on demand rather than applied uniformly. Crucially, $N=5$ is an ex-post optimum found by grid search on the same test distribution; on an unseen dataset it may be suboptimal, whereas adaptive triggering requires no such tuning. Evaluating the Adaptive RAG model without any context at inference (last row) causes a sharp degradation to 0.402; this out-of-distribution result confirms that the model has formed a genuine dependence on retrieved context, and is included for completeness rather than as a fair comparison.

5.5 Qualitative Analysis

Figure 3 illustrates how the representational bottleneck manifests and how retrieval compensates. The base model, relying solely on the impoverished visual embedding, hallucinates a long list of peripheral vascular structures (femoral, popliteal, and tibial arteries) that are outside the chest-CT field of view and implausible under non-contrast imaging—a direct consequence of the limited effective dimensions available in the visual channel. When the adaptive [RAG] trigger fires, the retrieved evidence supplies patient-specific context centred on the aortic arch and coronary arteries; the model then regenerates the sentence, correctly focusing on aortic arch calcification and coronary vascular involvement, which aligns with the ground truth. This example illustrates that retrieval does not merely re-rank information already present in the visual input; it introduces clinically specific evidence that the visual embedding alone cannot provide.

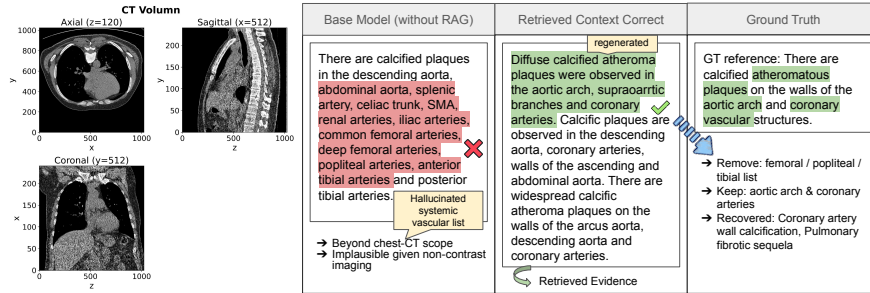


Fig. 3: Qualitative comparison for an aorta finding. Left: base model output; centre: AdaRAG-CT output with the regenerated sentence highlighted; right: ground-truth report. Red highlights indicate hallucinated content; green indicates correct clinical findings.

6 Discussion

Our results converge on a central finding: *the bottleneck in 3D CT report generation is representational, not generative*. The PCA analysis shows that contrastive embeddings carry as few as 2–9 effective dimensions of information; the scale experiment confirms that a 70B LLM cannot outperform an 8B model when both read the same impoverished visual channel. These observations reframe the role of RAG: rather than helping the LLM better utilise existing visual information, retrieval *opens a second, higher-bandwidth channel*, text tokens, through which fine-grained pathology semantics (laterality, severity, co-occurring findings) can reach the generator. This distinguishes our framework from conventional RAG systems designed to access external world knowledge or improve factual grounding in general-domain tasks; here, retrieval functions as a *surrogate visual channel*, compensating for information that the embedding simply fails to encode rather than supplementing an otherwise sufficient representation.

The framework design follows naturally from this perspective. The retrieval module opens the textual channel, supplying candidate sentences from the training corpus. The adaptive [RAG] trigger then controls this channel, ensuring context is consumed only when the model judges it useful; ablation studies confirm that fixed-interval injection is sensitive to frequency and cannot match adaptive triggering on NLP quality. This dynamic also explains the scale experiment: a 70B model equipped with stronger language priors produces more fluent text but, given the same impoverished visual signal, generates more confident hallucinations rather than better-calibrated outputs—retrieval corrects this by injecting patient-specific evidence that overrides generic priors. A key enabler of the adaptive mechanism is oracle-mixed training: by exposing the model to both high-quality oracle context and noisy retrieved context during training, it acts as implicit data augmentation, producing a generator that exploits retrieved evidence when it helps and falls back gracefully to visual-only generation when it does not.

Limitations. All experiments use CT-RATE, a single-institution dataset of non-contrast chest CT. While the cross-encoder analysis provides evidence of generality, validation on additional datasets and anatomical regions is needed. The oracle-mixed training regime introduces p_{oracle} as a hyperparameter whose optimal value may be dataset-dependent.

Our retrieval database is drawn entirely from the training corpus and introduces no external medical knowledge; its value lies in opening a supplementary textual channel rather than supplying genuinely new clinical information. A related limitation concerns context quality: many CT-RATE sentences follow highly standardized templates (e.g., “No evidence of pleural effusion”), which appear frequently in the database and may trigger the [RAG] mechanism without adding patient-specific evidence. More broadly, because database sentences share the same training distribution as the model’s parameters, retrieved context can reinforce corpus language patterns, causing outputs to converge toward common phrasing even when the visual evidence would support more specific descriptions.

The primary evaluation metric, Clinical F1, measures binary presence or absence of 18 predefined pathological categories but cannot capture the clinical richness of a well-formed radiology report. Critically, it does not assess lesion-level attributes—size, location, laterality, morphology, or severity grade—that are essential for clinical decision-making. A report that correctly flags “lung nodule” but provides no information about its size (3 mm vs. 15 mm) or location receives the same score as one that does. Temporal comparisons, follow-up measurement recommendations, and incidental findings outside the 18-label taxonomy are likewise invisible to this metric. Developing evaluation frameworks that measure the clinical completeness and quantitative accuracy of generated reports remains an important open problem.

AdaRAG-CT compensates for the representational bottleneck by routing supplementary information through a textual channel, but does not resolve the underlying cause. The dimensional collapse of contrastive embeddings arises from training on small medical datasets with limited pathological diversity; our retrieval framework provides a practical workaround rather than a fundamental fix. True resolution would require richer visual representations through pathology-aware pre-training or dense per-token visual features; until such encoders become available, the textual retrieval channel remains a necessary and effective surrogate.

7 Conclusion

3D CT contrastive embeddings, despite encoding pathology-discriminative signals, carry as few as 2 effective dimensions out of 512. This representational poverty—not the generator’s capacity—is the fundamental bottleneck: scaling the LLM from 8B to 70B parameters yields no improvement because both models read the same impoverished visual channel. AdaRAG-CT addresses this bottleneck by opening a supplementary textual channel through adaptive retrieval.

A learned [RAG] token triggers patient-specific context injection during generation, achieving a Clinical F1 of 0.480 on CT-RATE and surpassing the prior state of the art by 6.0 percentage points. Ablation studies confirm that the adaptive utilization mechanism, rather than the choice of retrieval pipeline, drives this improvement. Resolving the bottleneck at its source—through pathology-aware visual pre-training or dense per-token visual representations—remains the most important direction for future work. Until richer encoders become available, the textual retrieval channel provides a necessary and effective surrogate.

References

1. Aghajanyan, A., Gupta, S., Zettlemoyer, L.: Intrinsic dimensionality explains the effectiveness of language model fine-tuning. In: Annual Meeting of the Association for Computational Linguistics. pp. 7319–7328 (2021) [2](#), [4](#)
2. Alain, G., Bengio, Y.: Understanding intermediate layers using linear classifier probes. arXiv preprint arXiv:1610.01644 (2017) [2](#), [4](#)
3. Asai, A., Wu, Z., Wang, Y., Sil, A., Hajishirzi, H.: Self-RAG: Learning to retrieve, generate, and critique through self-reflection. In: International Conference on Learning Representations (2024) [2](#), [3](#), [8](#)
4. Bai, F., Du, Y., Huang, T., Meng, M.Q.H., Zhao, B.: M3D: Advancing 3D medical image analysis with multi-modal large language models. arXiv preprint arXiv:2404.00578 (2024) [3](#)
5. Banerjee, S., Lavie, A.: METEOR: An automatic metric for MT evaluation with improved correlation with human judgments. In: Proceedings of the ACL Workshop on Intrinsic and Extrinsic Evaluation Measures for Machine Translation and/or Summarization. pp. 65–72 (2005) [10](#)
6. Blankemeier, L., Cohen, J.P., Kumar, A., Van Veen, D., Gardezi, S.J.S., Paschali, M., Chen, Z., Delbrouck, J.B., Reis, E.P., Truys, C., et al.: Merlin: A vision language foundation model for 3d computed tomography. Research Square (2024) [10](#)
7. Boecking, B., Usuyama, N., Bannur, S., Castro, D.C., Schwaighofer, A., Hyland, S., Wetscherek, M., Naumann, T., Nori, A., Alvarez-Valle, J., et al.: Making the most of text semantics to improve biomedical vision–language processing. In: European Conference on Computer Vision. pp. 1–21. Springer (2022) [8](#)
8. Buckley, C.J., Almansoori, M., Azizi, A., Oikonomou, A., Vafaei Sadr, A., Apte, A., El Naqa, I.: LaB-RAG: Label boosted retrieval augmented generation for radiology report generation. arXiv preprint arXiv:2411.16523 (2024) [3](#)
9. Cao, W., Zhang, J., Shui, Z., Wang, S., Chen, Z., Li, X., Lu, L., Ye, X., Liang, T., Zhang, Q., Zhang, L.: Boosting vision semantic density with anatomy normality modeling for medical vision-language pre-training. arXiv preprint arXiv:2508.03742 (2025) [4](#)
10. Carbonell, J., Goldstein, J.: The use of MMR, diversity-based reranking for re-ordering documents and producing summaries. In: Proceedings of the 21st Annual International ACM SIGIR Conference on Research and Development in Information Retrieval. pp. 335–336 (1998) [8](#)
11. Chen, H., Zhao, W., Li, Y., Zhang, T., Wang, Z., Xu, D., Li, M., Ma, L.: CT-Agent: A multimodal-LLM agent for 3D CT radiology question answering. arXiv preprint arXiv:2505.16229 (2025) [1](#), [3](#), [10](#)

12. Chen, Z., Song, Y., Chang, T.H., Wan, X.: Generating radiology reports via memory-driven transformer. In: Proceedings of the 2020 Conference on Empirical Methods in Natural Language Processing (EMNLP). pp. 1439–1449 (2020) [3](#)
13. Gao, Y., Xiong, Y., Gao, X., Jia, K., Pan, J., Bi, Y., Dai, Y., Sun, J., Wang, H.: Retrieval-augmented generation for large language models: A survey. arXiv preprint arXiv:2312.10997 (2024) [2](#), [3](#)
14. Grattafiori, A., Dubey, A., Jauhri, A., Pandey, A., Kadian, A., Al-Dahle, A., Letman, A., Mathur, A., Schelten, A., et al.: The llama 3 herd of models. arXiv preprint arXiv:2407.21783 (2024) [7](#)
15. Hamamci, I.E., Er, S., Almas, F., Simsek, A.G., Esirgun, S.N., Dogan, I., Dasedelen, M.F., Durugol, O.F., Wittmann, B., Amiranashvili, T., et al.: Generalist foundation models from a multimodal dataset for 3D computed tomography. Nature Biomedical Engineering pp. 1–19 (2025) [1](#), [3](#), [4](#), [5](#), [9](#), [10](#), [21](#), [23](#)
16. Hamamci, I.E., Er, S., Menze, B.: CT2Rep: Automated radiology report generation for 3D medical imaging. In: International Conference on Medical Image Computing and Computer-Assisted Intervention (MICCAI). pp. 476–486. Springer (2024) [3](#), [10](#)
17. Hamamci, I.E., Er, S., Shit, S., Reynaud, H., Yang, D., Guo, P., Edgar, M., Xu, D., Kainz, B., Menze, B.: Better tokens for better 3D: Advancing vision-language modeling in 3D medical imaging. In: Advances in Neural Information Processing Systems (2025) [1](#), [2](#), [3](#), [5](#), [10](#)
18. Hosseini, A., Ibrahim, A., Serag, A.: From slices to volumes: Multi-scale fusion of 2D and 3D features for CT scan report generation. In: International Conference on Medical Image Computing and Computer-Assisted Intervention (MICCAI). Springer (2025) [3](#), [10](#)
19. Jeblick, K., Schachtner, B., Dexl, J., Mittermeier, A., Stüber, A.T., Topalis, J., Weber, T., Wesp, P., Sabel, B., Ricke, J., Ingrisch, M.: Retrieval-augmented generation with large language models in radiology. Radiology: Artificial Intelligence **7**(2) (2025) [2](#), [3](#)
20. Jiang, Z., Xu, F.F., Gao, L., Sun, Z., Liu, Q., Dwivedi-Yu, J., Yang, Y., Callan, J., Neubig, G.: Active retrieval augmented generation. In: Proceedings of the 2023 Conference on Empirical Methods in Natural Language Processing. pp. 7969–7992 (2023) [3](#)
21. Jing, L., Vincent, P., LeCun, Y., Tian, Y.: Understanding dimensional collapse in contrastive self-supervised learning. In: International Conference on Learning Representations (2022) [2](#), [4](#)
22. Lee, C., Park, S., Shin, C.I., Choi, W.H., Park, H.J., Lee, J.E., Ye, J.C.: Read like a radiologist: Efficient vision-language model for 3D medical imaging interpretation (2024), arXiv preprint arXiv:2412.13558 [3](#)
23. Lewis, P., Perez, E., Piktus, A., Petroni, F., Karpukhin, V., Goyal, N., Küttler, H., Lewis, M., Yih, W.t., Rocktäschel, T., Riedel, S., Kiela, D.: Retrieval-augmented generation for knowledge-intensive NLP tasks. In: Advances in Neural Information Processing Systems. vol. 33, pp. 9459–9474 (2020) [2](#)
24. Li, L., Cai, P., Rossi, R.A., Dernoncourt, F., Kveton, B., Wu, J., Yu, T., Song, L., Yang, T., Qin, Y., Ahmed, N.K., Basu, S., Mukherjee, S., Zhang, R., Hu, Z., Ni, B., Zhou, Y., Wang, Z., Huang, Y., Wang, Y., Zhang, X., Yu, P.S., Hu, X., Zhao, Y.: A personalized conversational benchmark: Towards simulating personalized conversations (2025), <https://arxiv.org/abs/2505.14106> [3](#)

25. Li, L., Ji, W., Wu, Y., Li, M., Qin, Y., Wei, L., Zimmermann, R.: Panoptic scene graph generation with semantics-prototype learning. Proceedings of the AAAI Conference on Artificial Intelligence **38**(4), 3145–3153 (Mar 2024). <https://doi.org/10.1609/aaai.v38i4.28098>, <https://ojs.aaai.org/index.php/AAAI/article/view/28098> **3**
26. Li, L., Wang, C., Qin, Y., Ji, W., Liang, R.: Biased-predicate annotation identification via unbiased visual predicate representation. In: Proceedings of the 31st ACM International Conference on Multimedia. p. 4410–4420. MM '23, Association for Computing Machinery, New York, NY, USA (2023). <https://doi.org/10.1145/3581783.3611847>, <https://doi.org/10.1145/3581783.3611847> **3**
27. Li, S., Cai, P., Zhou, Y., Ni, Z., Liang, R., Qin, Y., Nian, Y., Tu, Z., Hu, X., Zhao, Y.: Secure on-device video ood detection without backpropagation. In: International Conference on Computer Vision (ICCV) (October 2025) **4**
28. Li, S., Gong, H., Dong, H., Yang, T., Tu, Z., Zhao, Y.: Dpu: Dynamic prototype updating for multimodal out-of-distribution detection. In: Proceedings of the IEEE/CVF Conference on Computer Vision and Pattern Recognition (CVPR). pp. 10193–10202 (June 2025) **4**
29. Li, S., Rossi, R., Kim, S., Choudhary, S., Deroncourt, F., Mathur, P., Tu, Z., Zhao, Y.: Charts are not images: On the challenges of scientific chart editing (2025), <https://arxiv.org/abs/2512.00752> **3**
30. Li, S., Yu, C., Ni, Z., Li, H., Peris, C., Xiao, C., Zhao, Y.: Defenses against prompt attacks learn surface heuristics (2026), <https://arxiv.org/abs/2601.07185> **4**
31. Liang, W., Zhang, Y., Kwon, Y., Yeung, S., Zou, J.: Mind the gap: Understanding the modality gap in multi-modal contrastive representation learning. In: Advances in Neural Information Processing Systems. vol. 35, pp. 17612–17625 (2022) **4**
32. Lin, C.Y.: ROUGE: A package for automatic evaluation of summaries. In: Text Summarization Branches Out. pp. 74–81 (2004) **10**
33. Liu, H., Li, C., Wu, Q., Lee, Y.J.: Visual instruction tuning. Advances in Neural Information Processing Systems **36** (2024) **7**
34. Luo, L., Tang, B., Chen, X., Han, R., Chen, T.: VividMed: Vision language model with versatile visual grounding for medicine. In: Chiruzzo, L., Ritter, A., Wang, L. (eds.) Proceedings of the 2025 Conference of the Nations of the Americas Chapter of the Association for Computational Linguistics: Human Language Technologies (Volume 1: Long Papers). pp. 1800–1821. Association for Computational Linguistics, Albuquerque, New Mexico (Apr 2025). <https://doi.org/10.18653/v1/2025.naacl-long.89>, <https://aclanthology.org/2025.naacl-long.89/> **3**
35. Papineni, K., Roukos, S., Ward, T., Zhu, W.J.: BLEU: A method for automatic evaluation of machine translation. In: Proceedings of the 40th Annual Meeting of the Association for Computational Linguistics. pp. 311–318 (2002) **10**
36. Radford, A., Kim, J.W., Hallacy, C., Ramesh, A., Goh, G., Agarwal, S., Sastry, G., Askell, A., Mishkin, P., Clark, J., et al.: Learning transferable visual models from natural language supervision. In: International Conference on Machine Learning. pp. 8748–8763. PMLR (2021) **3**
37. Shawn, L., Qu, J., Song, L., Zhou, Y., Qin, Y., Yang, T., Zhao, Y.: Treble counterfactual VLMS: A causal approach to hallucination. In: Association for Computational Linguistics: EMNLP 2025. pp. 18423–18434. Association for Computational Linguistics, Suzhou, China (Nov 2025) **4**
38. Shui, Z., Zhang, J., Cao, W., Wang, S., Guo, R., Lu, L., Yang, L., Ye, X., Liang, T., Zhang, Q., Zhang, L.: Large-scale and fine-grained vision-language pre-training for enhanced CT image understanding. arXiv preprint arXiv:2501.14548 (2025) **4**

39. Tong, S., Liu, Z., Zhai, Y., Ma, Y., LeCun, Y., Xie, S.: Eyes wide shut? exploring the visual shortcomings of multimodal LLMs. In: IEEE/CVF Conference on Computer Vision and Pattern Recognition (2024) **2**
40. Wang, Z., Liu, L., Wang, L., Zhou, L.: METransformer: Radiology report generation by transformer with multiple learnable expert tokens. In: Proceedings of the IEEE/CVF Conference on Computer Vision and Pattern Recognition (CVPR). pp. 11558–11567 (2023). <https://doi.org/10.1109/CVPR52729.2023.01112> **3**
41. Wu, C., Zhang, X., Lin, W., Zhang, Y., Wang, Y., Xie, W.: Towards generalist foundation model for radiology by leveraging medical vision-language datasets. *Nature Communications* **16**(1), 5538 (2025) **3**
42. Xin, Y., Ates, G.C., Gong, K., Shao, W.: Med3dvlm: An efficient vision-language model for 3d medical image analysis. *IEEE Journal of Biomedical and Health Informatics* (2025) **3**
43. Yan, A., McAuley, J., Lu, X., Du, J., Chang, E.Y., Gentili, A., Hsu, C.N.: Radbert: Adapting transformer-based language models to radiology. *Radiology: Artificial Intelligence* **4**(4), e210258 (2022) **10**
44. Zhang, J., Lan, X., Qu, X., Cheng, Y., Feng, M., Hooi, B.: Learning the unlearned: Mitigating feature suppression in contrastive learning. In: European Conference on Computer Vision. pp. 37–54. Springer (2024) **4**

A Additional Evidence for the Embedding Bottleneck

A.1 PCA and linear probe protocol details

We evaluate representational bottleneck severity using both principal component analysis (PCA) and frozen linear probes. PCA is computed via full SVD on mean-centred embeddings. We report three effective-dimensionality metrics: dim_{90} and dim_{95} (the minimum number of principal components needed to explain 90% and 95% of total variance, respectively), and the participation ratio

$$\text{PR} = \frac{(\sum_i \sigma_i^2)^2}{\sum_i \sigma_i^4}, \quad (3)$$

where σ_i are the singular values. PR equals the embedding dimension when all dimensions carry equal variance and approaches 1 under complete collapse.

Linear probes are trained independently for each of the 18 CT-RATE pathology labels. Each probe is a logistic regression (solver: L-BFGS, $C=1.0$, class-balanced weighting, up to 1,000 iterations) trained on the training set and evaluated on the held-out validation set. Classification performance is reported as AUC-ROC.

A.2 Projection test details

To quantify variance-semantic misalignment, we perform a *projection test*: for each class or pathology, we train a linear probe on only the top- k or tail- k principal components of the embedding space and measure binary classification AUC. If the dominant variance directions encode class-discriminative information, the top- k probe should outperform the tail- k probe. A reversal (tail > top) indicates that discriminative signals reside in low-variance dimensions that cosine similarity effectively ignores.

Table 6 compares CLIP ViT-B/32 on ImageNet with the zero-shot CT-CLIP embedding used in our pipeline. Both domains exhibit the tail > top pattern, but the severity differs substantially. For CLIP, the top-2 PCs remain informative (AUC 0.82), whereas for CT-CLIP zero-shot the top-2 AUC is only 0.55, near random chance. This supports the claim that 3D medical contrastive embeddings suffer a much stronger form of variance-semantic misalignment than natural-image CLIP.

Table 7 shows the projection test for all 18 CT-RATE pathological findings on the zero-shot CT-CLIP embedding used in our pipeline. Every finding satisfies $\text{tail}_{1/2} > \text{top}_2$, confirming that the misalignment is not driven by only a few outliers.

B Implementation Details

B.1 Dataset and report preprocessing

We use the official CT-RATE split. Each study contains a Findings section and an Impression section; for report generation we concatenate both sections into

Table 6: Cross-domain projection test (mean over all classes or findings). top2: AUC using only the 2 highest-variance PCs. tail_{1/2}: AUC using the lower half of all PCs. Δ : tail_{1/2} - top2.

Domain / Model	top2 AUC	tail _{1/2} AUC	Δ
CLIP ViT-B/32 (ImageNet, 30 classes)	0.821	1.000	+0.178
CT-CLIP zero-shot, avg pool (CT-RATE, 18 findings)	0.552	0.746	+0.193
CT-CLIP zero-shot, max pool (CT-RATE, 18 findings)	0.533	0.739	+0.206

Table 7: Per-finding projection test on CT-CLIP zero-shot. All 18 pathological findings show tail_{1/2} > top2.

Finding	top2 AUC	tail _{1/2} AUC	Δ
Medical material	0.532	0.770	+0.238
Arterial wall calcification	0.514	0.708	+0.194
Coronary artery wall calc.	0.501	0.713	+0.212
Lymphadenopathy	0.519	0.677	+0.158
Lung nodule	0.545	0.651	+0.106
Pericardial effusion	0.514	0.817	+0.303
Hiatal hernia	0.525	0.748	+0.223
Mosaic attenuation	0.540	0.808	+0.268
Peribronchial thickening	0.571	0.755	+0.184
Consolidation	0.531	0.726	+0.195
Bronchiectasis	0.537	0.774	+0.237
Interlob. septal thickening	0.534	0.808	+0.274
Cardiomegaly	0.571	0.779	+0.208
Emphysema	0.521	0.711	+0.190
Atelectasis	0.536	0.709	+0.173
Lung opacity	0.542	0.672	+0.131
Pulm. fibrotic seq.	0.519	0.682	+0.163
Pleural effusion	0.535	0.787	+0.253

a single target sequence after basic text normalisation. The official training set contains 47,149 CT studies; we exclude 742 studies for which pre-computed organ embeddings are unavailable, leaving 46,407 training studies used in all experiments. The validation set contains 2,987 studies, all of which have corresponding embeddings.

For retrieval database construction, organ-level report paragraphs (produced by a rule-based organ-section parser) are sentence-split by a regex tokeniser that segments on full stops and semicolons followed by whitespace. Fragments consisting solely of punctuation or bare organ-name headers are discarded. Sentences that do not map cleanly to the four target organs are assigned to an *other* category and excluded from the retrieval indices. The final per-organ sentence database is built from training studies only; Tab. 8 summarises its composition. Reassembling the organ-split paragraphs yields BLEU-1 = 0.992 against the orig-

inal report, and per-organ Clinical F1 (Parser F1 in Tab. 8) exceeds 0.95 for all four target organs, confirming faithful preservation of pathological content.

Table 8: Per-organ sentence database statistics (training set only).

Organ	Sentences	Unique studies	Avg. sents/study	Avg. words/sent	Parser F1
Lung	398,538	46,380	8.59	13.3	0.974
Heart	82,025	42,777	1.92	8.4	0.957
Esophagus	50,096	39,977	1.25	11.8	0.990
Aorta	41,632	25,093	1.66	10.0	0.955
Total	572,291	—	—	—	—

B.2 Training, evaluation, and checkpoint selection

Clinical efficacy follows the CT-RATE protocol [15]: a RadBERT classifier extracts 18 binary findings per report, and we report support-weighted Precision, Recall, and F1. BLEU, ROUGE-L, and METEOR are computed after lower-casing. LLaMA Score uses Llama-3.1-70B-Instruct as judge. Bootstrap 95% CIs use 1,000 iterations. Both the 8B and 70B models follow the same two-stage training recipe: (1) train organ-specific projectors with the LLM frozen, then (2) LoRA fine-tune the language model jointly with the projectors. The base visual input comprises one global CT-CLIP embedding and four organ-specific ViSD-Boost embeddings, projected to the LLM hidden dimension by independent two-layer MLPs. All reported validation results correspond to the manually selected checkpoint with the best Clin-F1 on the validation set. To isolate whether the bottleneck lies in the generator or in the visual representation, the 8B and 70B variants are trained with the same visual interface, the same projector design, and the same evaluation protocol; both models receive the same five visual tokens, differing only in LLM scale.

B.3 RAG token supervision and oracle-mixed training

A dedicated [RAG] token is appended to the tokenizer vocabulary and fine-tuned jointly with the generation objective (LoRA $r=32$, $\alpha=64$, $\text{lr}=10^{-5}$, effective batch size 16, cosine schedule with 200 warmup steps). During training, oracle context is injected periodically (roughly every 2–3 sentences) before target sentences: 1–2 ground-truth sentences drawn from later in the same report are wrapped in `<|ret_start|> . . . <|ret_end|>` delimiters and prepended to the current generation position. Context tokens are masked from the language modelling loss (labels set to -100) so that the model learns to *condition on* retrieved text rather than reproduce it. The oracle-mixed ratio p_{oracle} controls how often oracle (vs. real-retrieved) context is used. In our best model (AdaRAG-CT / P10), $p_{\text{oracle}}=0.7$ and at most $K_{\text{rag}}=4$ [RAG] triggers are allowed per training

Table 9: Per-finding Clinical F1 breakdown: base model (8B, no RAG) vs. AdaRAG-CT (8B, two-stage). Δ : change due to adaptive retrieval augmentation.

Finding	Base F1	AdaRAG F1	Δ
<i>Lung findings (11)</i>			
Lung nodule	0.565	0.591	+0.025
Mosaic attenuation	0.349	0.379	+0.030
Peribronch. thick.	0.245	0.160	-0.085
Consolidation	0.524	0.534	+0.009
Bronchiectasis	0.096	0.151	+0.054
Interlob. septal thick.	0.251	0.343	+0.092
Emphysema	0.433	0.410	-0.023
Atelectasis	0.437	0.436	-0.001
Lung opacity	0.651	0.677	+0.027
Pulm. fibrotic seq.	0.275	0.475	+0.200
Pleural effusion	0.641	0.748	+0.107
<i>Heart findings (2)</i>			
Cardiomegaly	0.440	0.452	+0.012
Pericardial effusion	0.112	0.132	+0.020
<i>Aorta findings (2)</i>			
Arterial wall calc.	0.654	0.688	+0.034
Coronary artery calc.	0.592	0.666	+0.073
<i>Esophagus findings (1)</i>			
Hiatal hernia	0.261	0.358	+0.097
<i>Other findings (2)</i>			
Lymphadenopathy	0.329	0.207	-0.122
Medical material	0.240	0.066	-0.174
Weighted avg (Clin-F1)	0.455	0.480	+0.025

sample. This regime provides high-quality supervision signals while exposing the model to realistic retrieved context in the remaining 30% of cases.

C Additional Results

C.1 Per-finding clinical F1 breakdown

Table 9 decomposes the aggregate Clinical F1 improvement into individual pathological findings. AdaRAG-CT improves F1 on 13 of 18 findings. The largest gains occur for findings that require fine-grained descriptive detail: pulmonary fibrotic sequela (+0.200), pleural effusion (+0.107), and hiatal hernia (+0.097). These are findings where the base model’s impoverished visual channel fails to encode sufficient detail, and the retrieved textual context supplies the missing semantics. The few regressions (medical material -0.174, lymphadenopathy -0.122) involve low-prevalence findings whose retrieval candidates are sparse or dominated by negative templates.

Table 10: Reproduced baselines under our unified evaluation protocol (CT-RATE validation set).

Method	Params	Clinical Efficacy			NLP				LLaMA
		F1	P	R	B-1	B-4	R-L	MET	
CT-CHAT [15]	8B	0.224	0.331	0.366	0.421	0.188	0.303	0.193	6.73
CT-CHAT [15]	70B	0.161	0.334	0.131	0.356	0.182	0.321	0.190	6.02
Ours (base)	8B	0.455	0.474	0.469	0.463	0.205	0.315	0.206	7.30
AdaRAG-CT	8B	0.480	0.502	0.520	0.496	0.242	0.354	0.246	7.75
Ours (base)	70B	0.405	0.468	0.373	0.449	0.213	0.334	0.208	7.10
AdaRAG-CT	70B	0.426	0.483	0.413	0.497	0.250	0.361	0.232	7.53

C.2 Adaptive trigger statistics

On the CT-RATE validation set (2,987 reports), the 8B AdaRAG-CT model emits an average of 1.48 [RAG] triggers per report (median 1). 22% of reports receive zero triggers, indicating that the model judges retrieval unnecessary for straightforward cases, while 61% receive 1–2 triggers and 17% receive 3 or more. Nearly all triggers fire during the lung paragraph, the organ with the lowest retrieval precision and the highest number of distinct findings. This confirms that the adaptive mechanism has learned to concentrate retrieval where the visual bottleneck is most severe.

C.3 Reproduced baselines

To ensure a fair comparison under consistent evaluation conditions, we reproduce CT-CHAT under our evaluation pipeline and report all metrics alongside our own models in Tab. 10. The relative ranking is preserved under our protocol, while our base and adaptive models remain substantially stronger on clinical efficacy.